International Journal of Computational Methods and Experimental Measurements
https://www.acadlore.com/journals/IJCMEM

A Data-Driven and Experimental Approach to Thermal Risk Assessment in High-Current Electric Vehicle Power Cable Systems

Safarudin Gazali Herawan*, Azqy Nur Farenzy Saputra, Sharon Yemima, Bangkit Pramesta Yulianto

Department of Industrial Engineering, Faculty of Engineering, Bina Nusantara University, 11480 Jakarta, Indonesia

* Correspondence: Safarudin Gazali Herawan (safarudin.gazali@binus.edu)

Received: 10-28-2025 **Revised:** 12-12-2025 **Accepted:** 12-24-2025

Citation: S. G. Herawan, A. N. F. Saputra, S. Yemima, and B. P. Yulianto, "A data-driven and experimental approach to thermal risk assessment in high-current electric vehicle power cable systems," *Int. J. Comput. Methods Exp. Meas.*, vol. 13, no. 4, pp. 971–992, 2025. https://doi.org/10.56578/ijcmem130415.

Abstract: The increasing adoption of electric vehicles with fast-charging capability has intensified thermal challenges in power cables, potentially leading to localized overheating and reduced system reliability and service life. To address this issue, an integrated framework combining experimental measurement and data-driven analysis was developed to identify and predict thermal behaviour in critical electrical components of electric vehicles. A laboratory-scale electric vehicle powertrain was constructed to replicate representative operating conditions. Infrared thermography was employed together with synchronized electrical measurements to capture the coupled electrical–thermal response of the system. The powertrain was tested under variable mechanical loads ranging from 0% to over 80% and under constant-current operation at 15 A for 30 minutes. Passive thermal management using phase change materials (PCMs), specifically beeswax and paraffin, was evaluated to assess its effectiveness in mitigating temperature rise. In addition, a lightweight artificial neural network (ANN) model was developed to predict the temperatures of thermally critical components. Thermographic results showed that thermal stress was spatially concentrated at specific interfaces. At maximum load, the temperatures of the power cable downstream of the main switch, the motor cable, and the connector reached 41.2 ℃, 39.7 ℃, and 47 ℃, respectively. Analysis of battery charging behaviour revealed a strong correlation between battery temperature and charging current, with a correlation coefficient of 0.95. When PCMs were applied, the battery temperature rise was reduced to approximately 35.2–35.5 ℃, compared with 36.7 ℃ in the absence of PCMs, and voltage stability was improved. The ANN demonstrated high predictive accuracy, with R^2 values of 0.978 for main switch temperature, 0.969 for connector temperature, and 0.962 for motor cable temperature, corresponding to prediction errors within ±2.5 ℃ across all load conditions. These findings indicate that an integrated experimental and predictive diagnostic approach can effectively support thermal management and early risk identification in high-current electric vehicle power cable systems.

Keywords: Electric vehicle thermal management; High-current power cables; Thermographic analysis; Phase change materials; Artificial neural networks; Predictive thermal diagnostics

1 Introduction

Driven by the increasing demand for high-speed charging infrastructure and advances in battery technology, governments worldwide are implementing progressively stricter vehicle emission regulations. As electric vehicle adoption continues to grow, the efficient transfer of electrical power within vehicles has become increasingly critical. High-current electrical connections are widely employed to accelerate power transfer in electric vehicles. Although these systems enhance usability and charging convenience, they also introduce significant thermal challenges that adversely affect system reliability, safety, and operational lifespan. As electrical current increases within vehicle wiring and components, resistive heating intensifies and can no longer be regarded as a secondary concern. Instead, thermal stress has emerged as a major limiting factor in electric vehicle performance [1, 2]. Consequently, maintaining appropriate operating temperatures within electrical systems has become a central focus of ongoing research.

In electric vehicle electrical systems, thermal stress produces long-term effects that extend beyond immediate temperature elevation. Repeated overheating events accelerate insulation aging, increase resistive energy losses, and ultimately raise the likelihood of system failure, thereby posing serious safety risks [3, 4]. Unlike conventional vehicles dominated by internal combustion engines, electric vehicles concentrate substantial electrical power within

compact spatial constraints. Operating conditions such as charging, braking, and fluctuating driving demands impose highly variable electrical loads. Under these conditions, peripheral components including power cables, terminals, main switches, and circuit breakers often fail unexpectedly. Even when battery packs remain within prescribed temperature limits, localized heating and increased electrical resistance within individual cells or interfaces can generate hotspots [5, 6]. Ensuring the reliability of electric vehicles therefore requires a comprehensive understanding of thermally induced degradation mechanisms in peripheral electrical components.

The fundamental origin of thermal stress in electrical devices is Joule heating generated by current flow. This heating effect increases with the square of the current, making it particularly severe during high-current charging scenarios involving hundreds of amperes [1]. In conductors and connectors, heat generation not only raises surface temperatures but also induces steep thermal gradients within insulation layers and at electrical interfaces. Such gradients accelerate the aging of insulation materials, including cross-linked polyethylene (XLPE), which is highly sensitive to thermal ageing [7]. Experimental studies and numerical models have demonstrated that elevated temperatures promote the scission of long polymer chains within insulation materials, thereby reducing dielectric strength and increasing susceptibility to electrical discharges [2, 3]. This degradation process often evolves into a self-reinforcing cycle in which localized faults induce heating, accelerate insulation breakdown, and increase the probability of catastrophic failure [6].

Insulation breakdown caused by partial discharge represents a major failure mechanism in electrical power systems, particularly in high-voltage cable applications. Partial discharges frequently originate from imperfections such as voids, inclusions, or interfacial delamination within insulating layers. These defects locally intensify electric fields, producing micro-discharges that generate both heat and chemically reactive byproducts [7]. The activity of partial discharge is strongly temperature dependent, indicating that electrical and thermal stresses are closely coupled [2]. Repeated partial discharge events can progress into electrical treeing, resulting in irreversible insulation damage and eventual connector or cable failure. In electric vehicles, where high-energy battery systems are in close proximity, such failures may trigger cascading thermal runaway events [8, 9].

Within this context, connectors and main switches are particularly vulnerable to thermal degradation. As critical interfaces between cables and electrical equipment, connectors are susceptible to increased contact resistance arising from surface corrosion, mechanical wear, and manufacturing variability. These effects lead to localized heating that may remain difficult to detect due to non-uniform heat distribution [10, 11]. Vibration and thermal cycling further exacerbate this issue by inducing fretting wear, which generates debris and oxide layers that degrade contact integrity [12, 13]. Main switches similarly contribute to thermal stress through switching losses and repeated thermal cycling, which can induce fatigue in conductive and insulating materials and reduce operational reliability [14, 15].

To mitigate thermal risks, a range of cooling strategies has been proposed. Advanced cooling approaches, including liquid cooling and liquid immersion, are highly effective at dissipating heat from high-power components under heavy load conditions [9, 16]. However, active thermal management systems increase system complexity, cost, and energy consumption. Parallel research efforts have focused on developing materials and composite structures capable of withstanding higher temperatures while maintaining electrical integrity [17, 18]. Although material-level improvements have achieved notable progress, effective techniques for early detection and diagnosis of thermal degradation prior to catastrophic failure remain limited.

Thermal monitoring therefore plays a critical role in electric vehicle safety and reliability. Infrared thermography is a widely adopted non-contact technique for surface temperature measurement and has proven effective in identifying localized hotspots within electric vehicle powertrain components [19]. Nevertheless, infrared methods are primarily limited to surface temperature assessment and may not reveal internal defects or subsurface thermal conditions, particularly in components with complex geometries or multilayer insulation structures [20]. Measurement accuracy is also influenced by environmental conditions and material emissivity, while data interpretation depends heavily on operator expertise [21, 22]. Consequently, conventional inspection, repair, and replacement strategies remain largely reactive and are typically implemented during scheduled maintenance rather than continuous real-time monitoring.

Phase change materials (PCMs) have attracted increasing attention as passive thermal management solutions in electric vehicles. By absorbing latent heat during phase transitions, PCMs can limit peak battery temperatures, reduce thermal gradients, and improve temperature uniformity, thereby enhancing battery safety and cycle life [23, 24]. However, existing research has predominantly focused on battery-level applications, often overlooking other system components such as cables, connectors, and switches. Moreover, conventional heat sinks suffer from limitations including low thermal conductivity, potential leakage, and delayed thermal response under rapidly varying loads, which restrict their effectiveness in protecting electrical equipment [25, 26]. As a result, PCM-based approaches alone are insufficient for comprehensive thermal risk mitigation in electric vehicle power distribution systems.

Artificial neural networks (ANNs) and machine learning techniques have emerged as promising tools for fault diagnosis and thermal prediction in electric vehicles. Data-driven models can capture complex nonlinear relationships between electrical operating parameters and thermal behaviour, enabling early detection of abnormal operating conditions [27, 28]. Deep neural networks have demonstrated high accuracy in temperature prediction, fault

classification, and remaining useful life estimation across power electronics and battery systems [18, 29]. However, their substantial computational demands, limited interpretability, and insufficient experimental validation hinder deployment in real-time, safety-critical electric vehicle applications [30, 31].

Despite these advances, a significant research gap remains. Existing studies typically address thermal measurement, passive thermal management, or data-driven prediction in isolation, resulting in fragmented solutions that fail to capture the coupled thermal–electrical behaviour of electric vehicle power cable systems. Integrated frameworks that combine empirical hotspot identification, evaluation of PCM-based thermal buffering, and real-time prediction using experimentally validated and computationally efficient models remain scarce [32, 33]. Addressing this gap is essential for advancing predictive maintenance strategies and enhancing the reliability and safety of electric vehicle electrical systems.

In this study, an integrated thermal diagnostic and predictive framework for high-current electric vehicle power cable systems is developed. Thermographic analysis is combined with passive thermal management using PCMs and a lightweight ANN to enable real-time temperature prediction of critical components. The study provides four main contributions. First, it presents experimental characterization of the thermal behaviour of electric vehicle power cables, connectors, and switches under varying load conditions. Second, it evaluates the influence of thermal energy storage materials on battery performance and peripheral component temperatures. Third, it develops a computationally efficient method for real-time temperature prediction at the component level. Fourth, it validates the proposed framework through combined experimental data, statistical analysis, and predictive modelling. By integrating thermal, electrical, and mechanical considerations, this work aims to provide a practical and adaptable predictive thermal management approach for next-generation electric vehicle electrical systems.

2 Methodology

This study adopted an experimental methodology to replicate the thermal–electrical operating environment of electric vehicle motor and charging cable systems under representative conditions. A laboratory-scale electric vehicle powertrain test rig was developed to enable controlled experimentation, while thermal and electrical performance data were recorded synchronously. The powertrain was subjected to systematically defined operating scenarios to capture both transient and steady-state thermal responses. The experimental design and measurement procedures were established in accordance with well-documented approaches in electric vehicle thermal management and electro-thermal diagnostics reported in the literature [1, 2, 19].

2.1 Electric Vehicle Powertrain Test Bench

A laboratory-based test bench was constructed to simulate the electrical power distribution system of an electric vehicle operating under high-current conditions. The core of the test rig consisted of a 1500 W brushless direct current (DC) motor representative of those commonly employed in electric vehicle traction systems. The motor was powered by a custom-built lithium-ion battery pack configured in a thirteen-cell series arrangement, producing a moderate DC voltage comparable to that of practical electric vehicle subsystems. This configuration enabled realistic current flow through cables, connectors, and peripheral components during operation, consistent with previous experimental studies on electric vehicle powertrains [5, 15].

The primary components selected for thermal investigation included the motor, main power switch, motor controller, power cables, and associated electrical connectors. These components were deliberately chosen due to their known susceptibility to Joule heating, contact resistance effects, and thermal cycling, which have been identified as major contributors to thermal risk and reliability degradation in electric vehicles [6, 10]. The overall layout of the test bench was designed to closely replicate real-world vehicle electrical installations, thereby ensuring that thermal behaviour observed during testing reflected practical operating conditions. A schematic representation of the experimental configuration is provided in Figure 1, while a photograph of the assembled test rig is shown in Figure 2.

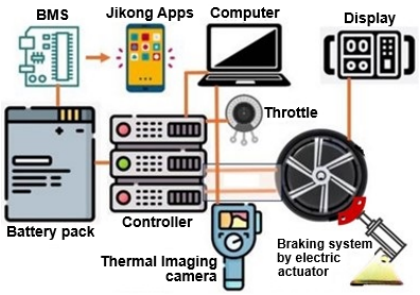

Figure 1. The schematic diagram of experimental setup

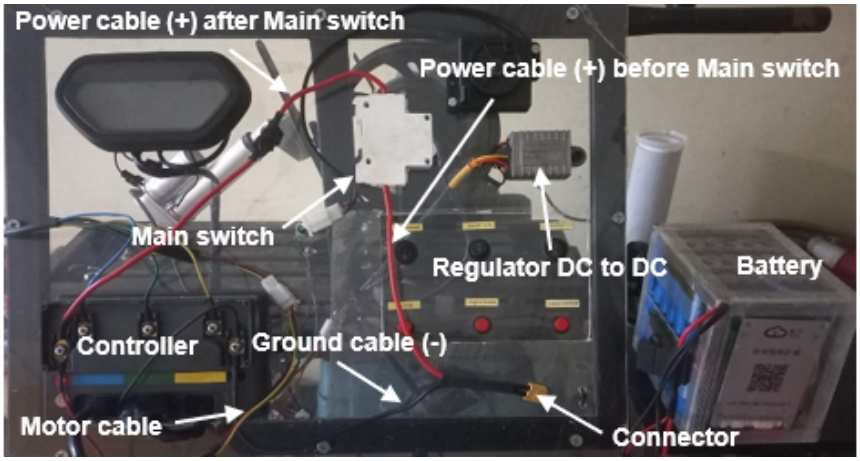

Figure 2. The experimental rig with components

To enable controlled variation of mechanical loading, the motor was coupled to an electrically powered braking system. This braking actuator allowed repeatable adjustment of the mechanical load by regulating the motor current, while maintaining stable and reproducible operating conditions. By modifying the braking force, the test bench simulated a range of driving and charging scenarios, including partial load, high load, and overload conditions. This approach is commonly adopted in electric vehicle thermal studies, as it generates consistent thermal stress profiles while avoiding the confounding influence of uncontrolled transient effects [1, 2]. The specific braking mechanism employed in this study is illustrated in Figure 3.

Figure 3. The electric actuator for braking mechanism system

2.2 Instrumentation and Data Acquisition

The instrumentation and data acquisition system were designed to capture high-resolution thermal and electrical measurements from all critical components in real time. Non-contact infrared thermography was employed for temperature measurement to avoid interference with electrical operation and to enable spatially resolved thermal analysis. A thermal imaging camera with a measurement range of 20 ℃ to 550 ℃ and a stated accuracy of ±2 ℃ was used consistently throughout the experiments, following established thermal testing protocols reported in the literature [19, 20].

Thermal inspections were conducted sequentially at predefined time intervals, focusing on components with elevated thermal risk, including the battery pack, motor controller, main switch, cable connectors, and power cables. These locations were selected due to their exposure to high current density, switching losses, and contact resistance, all of which are known contributors to localized heating in electric vehicle power distribution systems [10, 11]. The resulting thermographic images enabled both qualitative identification of hotspots and quantitative assessment of temperature evolution across components.

Electrical parameters were monitored continuously and synchronously with thermal imaging. Current and voltage data were supplied directly by the motor controller and battery management system, providing an accurate

representation of instantaneous electrical loading. The battery capacity ratio, defined as the remaining usable capacity relative to the initial capacity, was recorded for each test, together with the battery state of charge. These electrical measurements are essential for power cable and connector thermal analysis, as current magnitude and voltage stability have been shown to strongly influence temperature rise in electric vehicle electrical systems [3, 7].

Thermal and electrical data streams were logged synchronously using a centralized data acquisition computer. This temporal alignment enabled subsequent correlation analysis and supported the development, training, and validation of ANN models. In contrast, standalone thermal monitoring approaches often lack synchronization with electrical operating conditions, limiting their diagnostic value, as noted in reference [22].

2.3 Experimental Scenarios

The experimental programme was structured to examine load-dependent thermal behaviour and to evaluate the effectiveness of passive thermal management strategies under three representative operating scenarios. The first scenario involved incremental adjustment of the braking mechanism to progressively increase the motor load, generating load levels ranging from 0% to approximately 80% of the motor's rated capacity. These controlled loading steps produced corresponding increases in current flow through the power cables and connectors, thereby inducing measurable thermal stress. Previous studies have demonstrated the importance of load variation for identifying overheating locations and characterizing the relationship between electrical demand and temperature rise [1, 2].

The second scenario consisted of a constant-current test designed to investigate thermal behaviour under prolonged electrical stress. Following an initial stabilization period, the system was operated at a steady discharge current of approximately 15 A for a duration of 30 minutes. This condition reflects moderate real-world operating scenarios such as urban driving or daily commuting. Continuous thermal and electrical data acquisition during this period enabled analysis of transient heating behaviour, thermal stabilization, and steady-state temperature levels. Constant-current testing is widely employed in battery and cable thermal studies to isolate cumulative heating effects from load-induced fluctuations [23, 24].

The third scenario evaluated the influence of PCMs on system thermal behaviour. A baseline battery configuration without PCM was compared against battery assemblies integrated with beeswax PCM and paraffin PCM. These materials were selected based on their thermophysical properties and documented use in electric vehicle battery thermal management applications [23, 25]. Both materials exhibit latent heat storage capabilities and melting temperature ranges that overlap with typical lithium-ion battery operating conditions.

Beeswax PCM was selected due to its relatively high latent heat capacity and chemical stability, enabling thermal energy absorption through combined sensible and partial latent heat mechanisms. Experimental studies have shown that beeswax-based PCMs can moderate battery temperature rise within approximately 25–55 ℃, although its melting point lies slightly above the recommended battery operating window, resulting in predominantly sensible heat absorption under moderate loads [25]. Nevertheless, beeswax has demonstrated measurable thermal buffering and is widely regarded as a viable natural PCM for passive battery cooling.

Paraffin PCM was selected because its melting temperature aligns more closely with the optimal battery operating range, allowing more effective utilization of latent heat during sustained discharge. Prior investigations have reported that paraffin-based PCMs typically exhibit melting temperatures between 38 ℃ and 45 ℃, high latent heat capacity, and stable thermal behaviour, enabling more effective suppression of peak battery temperatures under continuous load conditions [23]. Paraffin has therefore been extensively applied in electric vehicle battery thermal management systems. The thermophysical properties of the selected PCMs are summarized in Table 1.

Table 1. Thermophysical properties of selected phase change materials (PCMs) for electric vehicle battery thermal management [34, 35]

Property	Beeswax PCM	Paraffin PCM
Typical melting point (℃)	62	38–45
Latent heat (kJ/kg)	141–145	200–250
Thermal conductivity ($W \cdot m^{-1} \cdot K^{-1}$)	0.25	0.20–0.30
Density (kg/m^3, solid)	820	800
Primary heat storage mode	Sensible + limited latent	Sensible + latent
Reported electric vehicle battery application	Passive battery cooling	Passive battery cooling

In this study, PCM integration was limited exclusively to the battery compartment, while all peripheral power distribution components remained unchanged. This configuration enabled isolated assessment of battery-level passive thermal management and its indirect influence on peripheral component temperatures. As a result, a clear distinction

could be made between battery core thermal regulation and interface-driven heating mechanisms elsewhere in the power distribution system.

Overall, the experimental methodology enabled the generation of a comprehensive dataset spanning variable load conditions, prolonged operation, and passive thermal management configurations. This dataset formed the basis for subsequent thermal diagnostics, statistical correlation analysis, and the development of lightweight predictive models suitable for real-time electric vehicle applications. The battery configurations employed are illustrated in Figure 4, and the key specifications of the experimental apparatus are summarized in Table 2.

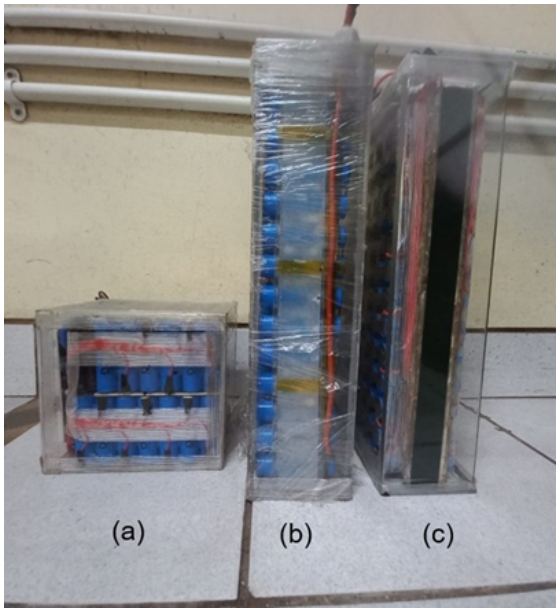

Figure 4. The battery pack configurations: (a) no phase change material (PCM); (b) paraffin PCM; (c) beeswax PCM

Table 2. Research summary of organizations

No.	Equipment	Specification
1	Brushless direct current (BLDC) motor	1500 W
2	SiAECOSYS VOTOL controller	50 A
3	Battery pack with 13 series of 6 batteries. Total 78 batteries	48 V 15 A
4	Throttle	Potentiometer with spring
5	Display	Revolutions per minute (RPM), Speed and Battery capacity
6	Jikong battery management system (BMS)	Voltage sensor for 13 series battery and battery temperature
7	InfiRay P2 Pro thermal camera	–20 ℃ to 550 ℃

3 Results

3.1 Thermographic Mapping of Cable Components

The thermographic frames presented in Figure 5 visually corroborate the quantitative measurements by revealing progressively intensified thermal signatures concentrated at the connector region and extending into the downstream cable segment as load increases. Thermographic mapping demonstrated a clear load-dependent escalation of temperature within the electric vehicle power cable system, accompanied by pronounced spatial non-uniformity in thermal behaviour. At the initial no-load condition, all monitored components exhibited surface temperatures of approximately 30 ℃, indicating negligible resistive heating under zero-current operation. As mechanical load was systematically increased through controlled braking, measurable temperature rises developed along the power transmission path, ultimately leading to the formation of localized hotspots.

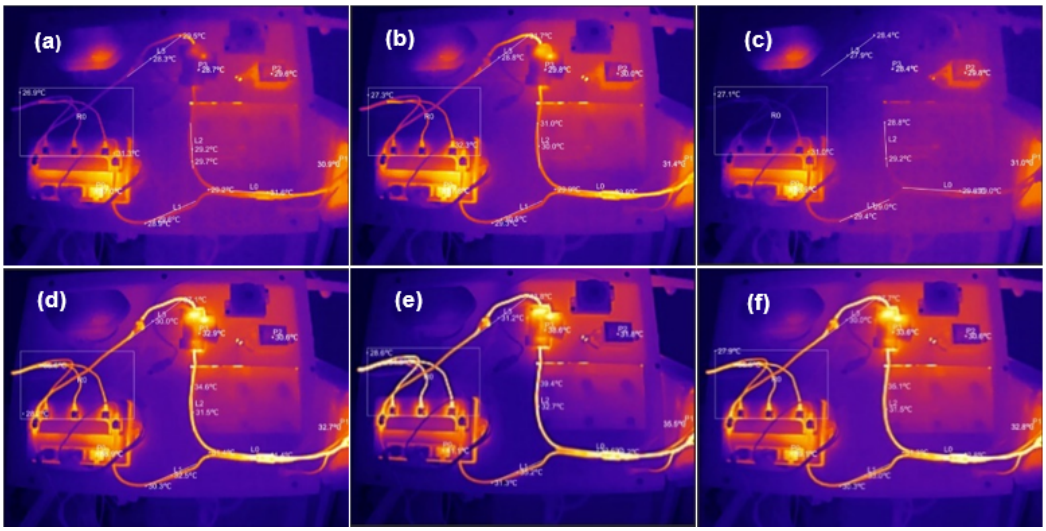

Figure 5. Thermographic frames of temperature in components under increasing load: (a) 0% load; (b) 20% load; (c) 40% load; (d) 60% load; (e) 80% load; (f) over 80% load

At moderate load levels of approximately 40–60% capacity, the connector temperature increased more rapidly than that of other components, exceeding 38 ℃, while the motor cable and power cable segments remained at or below 37 ℃. Under high-load conditions exceeding 80% of rated capacity, temperature differentials became increasingly pronounced. The connector reached a maximum surface temperature of 47 ℃, representing the highest thermal stress among all cable-related components. In comparison, the power cable segment downstream of the main switch reached approximately 41.2 ℃, the motor cable reached approximately 39.7 ℃, the upstream power cable reached approximately 37.4 ℃, and the main switch reached approximately 36.5 ℃. The temperature difference between upstream and downstream power cable segments across the main switch was particularly significant. Under high-load conditions, the downstream cable operated approximately 3.8 ℃ hotter than the upstream segment, reflecting additional thermal losses associated with switching interfaces and post-switch current flow. This downstream temperature amplification is consistent with previous studies showing that switching transitions and interface resistance elevate thermal stress in adjacent conductors, even when the switch housing itself does not exhibit the highest temperature [14, 15].

The motor cable exhibited intermediate thermal behaviour, with peak temperatures remaining 7.3 ℃ below the connector and 1.5 ℃ below the downstream power cable at maximum load. Although the motor cable experiences substantial resistive heating due to continuous current flow, its larger surface area promotes more effective heat dissipation compared to compact interface components. In contrast, the connector's limited geometry and elevated electrical contact resistance concentrate heat within a small volume, producing higher surface temperatures despite carrying comparable current.

Across all loading conditions, the thermographic measurements consistently followed a stable temperature hierarchy: connector (47 ℃), power cable after the main switch (41.2 ℃), motor cable (39.7 ℃), power cable before the main switch (37.4 ℃), and main switch (36.5 ℃). The persistence of this hierarchy across repeated load increments indicates that the observed thermal patterns are intrinsic to the system configuration rather than transient fluctuations. These findings align with prior thermographic and electro-thermal studies identifying electrical interfaces as dominant contributors to localized overheating in high-current electric vehicle power distribution systems [1, 2, 19].

3.2 Thermal Vulnerability Hierarchy

Quantitative analysis of thermographic data across all loading conditions enabled the establishment of a clear thermal vulnerability hierarchy among electric vehicle power cable components. The hierarchy was determined based on maximum surface temperatures recorded under high-load operation (>80% capacity) and on relative temperature differentials along the power transmission path. The peak temperatures and associated thermal differentials are summarized in Table 3.

Under peak load conditions, the electrical connector experienced the greatest thermal stress, reaching 47.0 ℃, which exceeded the main switch temperature by 10.5 ℃ and the upstream power cable temperature by 9.6 ℃. The downstream power cable segment exhibited the second-highest temperature at 41.2 ℃, followed by the motor cable at 39.7 ℃. In contrast, the upstream power cable and main switch reached lower peak temperatures of approximately 37.4 ℃ and 36.5 ℃, respectively.

Table 3. Peak temperatures and thermal differentials of electric vehicle power cable components under high-load conditions

Component	Peak Temperature (℃)	Temperature Difference vs. Connector (℃)
Connector	47.0	0.0
Power cable (+) after main switch	41.2	-5.8
Motor cable	39.7	-7.3
Power cable (+) before main switch	37.4	-9.6
Main switch	36.5	-10.5

The temperature differential of 5.8 ℃ between the connector and the downstream power cable indicates substantial thermal amplification at the connector interface. This observation supports the interpretation that electrical contact resistance is the dominant mechanism driving localized overheating, as interface regions dissipate heat less efficiently than bulk conductors. Previous studies have shown that even minor increases in contact resistance can produce disproportionately large temperature rises under high-current conditions, particularly in compact connector geometries [10, 11].

A pronounced asymmetry was also observed across the main switch. The downstream cable operated approximately 3.8 ℃ hotter than the upstream cable under identical current conditions, indicating that additional resistive and switching-related losses propagate into post-switch conductors. Similar behaviour has been reported in high-current switching devices, where thermal stress preferentially manifests in post-switch conductors rather than within the switch housing itself [14, 15].

The motor cable occupied an intermediate position in the hierarchy, operating 2.3 ℃ cooler than the downstream cable and 7.3 ℃ cooler than the connector at peak load. This reflects the balance between sustained resistive heating and enhanced heat dissipation resulting from its extended length and exposed surface area. In contrast, the compact geometry of connectors and junctions limits convective and radiative heat transfer, promoting localized temperature elevation.

The stability of this hierarchy across multiple load increments confirms that the observed thermal ranking is intrinsic to system design rather than a transient operating effect. This quantitative ordering is consistent with earlier studies identifying connectors, junctions, and post-switch regions as persistent thermal bottlenecks in high-current electric vehicle power distribution systems [1, 2, 19].

3.3 Electrical-Thermal Correlation Analysis

Pearson correlation coefficients were calculated to examine associations between component temperatures and three key electrical indicators: current, voltage ratio, and battery capacity ratio. The resulting correlations are visualized using lollipop charts in Figure 6 to facilitate direct comparison of correlation magnitude and direction across components. Pearson correlation (r) was employed as an exploratory diagnostic tool to characterize association strength rather than to infer causality, given the nonlinear and time-dependent nature of electro-thermal processes.

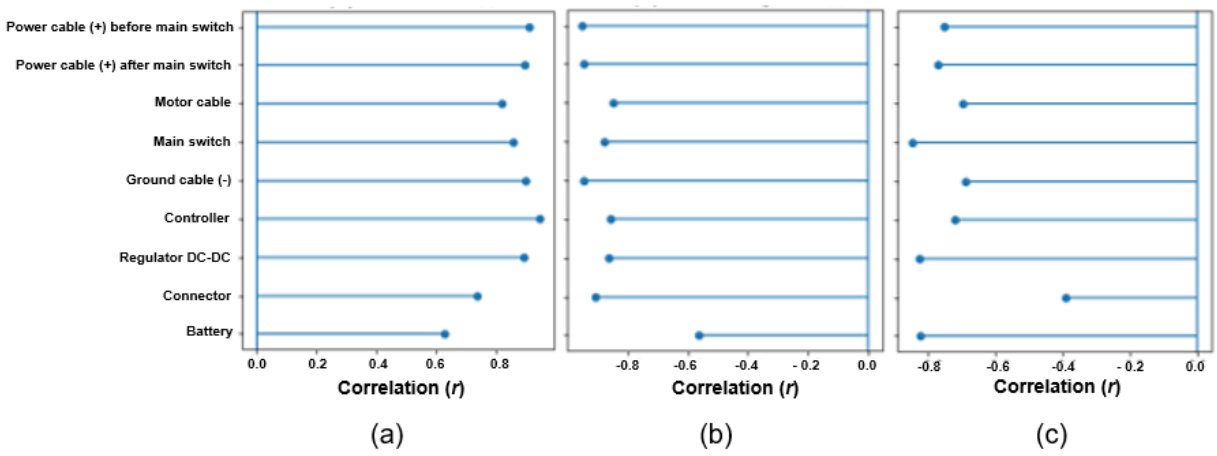

Figure 6. Lollipop charts showing the Pearson correlation coefficients (r) between component temperatures and key electrical parameters: (a) current (A), (b) voltage ratio (%), and (c) battery capacity ratio (%). Correlations were calculated based on n = 14 experimental operating points. All temperatures are expressed in degrees Celsius (℃)

As shown in Figure 6a, all components exhibited positive correlations between temperature and current, with coefficients ranging from r = 0.628 for the battery to r = 0.946 for the controller. Strong associations were observed for the controller (r = 0.946), power cable before the main switch (r = 0.910), ground cable (r = 0.900), and DC–DC regulator (r = 0.892). These results confirm that current is the dominant electrical indicator associated with temperature rise, consistent with Joule heating behavior, where generated heat scales with the square of current magnitude.

Figure 6b shows consistently negative correlations between component temperatures and voltage ratio, with coefficients ranging from r = -0.563 to r = -0.952. The strongest negative correlations were observed for the power cable before the main switch (r = -0.952), power cable after the main switch (r = -0.947), ground cable (r = -0.949), and connector (r = -0.909). These trends indicate that voltage ratio reductions often reflecting increased resistive losses are strongly associated with elevated temperatures, particularly along the main power path.

Similarly, Figure 6c reveals negative correlations between temperature and battery capacity ratio. The strongest associations were observed for the main switch (r = -0.846), DC–DC regulator (r = -0.826), battery (r = -0.825), and power cable after the main switch (r = -0.771), while the connector showed the weakest correlation (r = -0.391). This pattern suggests that reduced battery capacity ratio, indicative of increased internal resistance or aging effects, coincides with higher thermal stress in several components, whereas connector heating remains primarily governed by local contact resistance and current flow.

Collectively, Figure 6 provides a comparative assessment of thermal sensitivity across system components. Current emerges as the dominant stress indicator, while voltage ratio and battery capacity ratio act as secondary diagnostic indicators associated with resistive loss and battery condition. These findings support the selection of physically meaningful inputs for the predictive model developed in subsequent sections.

3.4 Peripheral Component Thermal Response

Quantitative analysis revealed that PCM integration within the battery enclosure had minimal influence on the thermal behaviour of peripheral components external to the battery pack. Across all configurations which no PCM, beeswax PCM, and paraffin PCM, the controller, main switch, and connector exhibited nearly identical temperature evolution profiles during the 30-minute constant-current discharge at 15 A. Final peripheral component temperatures are summarized in Table 4.

Table 4. Final peripheral component temperatures under constant-current discharge (15 A, 30 minutes)

Component	No PCM (℃)	Beeswax PCM (℃)	Paraffin PCM (℃)
Controller	40.4	39.8	39.4
Main switch	44.0	43.2	43.0
Connector	41.2	40.6	40.4
Fuse connector	51.0	51.0	<51.0*

Note: *Lower fuse connector temperature in the paraffin phase change material (PCM) case was attributed to thermal camera misalignment and is not interpreted as a confirmed thermal improvement.

The controller temperature remained within a narrow range of 39.4–40.4 ℃ across all configurations. The no-PCM configuration reached 40.4 ℃, while beeswax PCM and paraffin PCM stabilized at 39.8 ℃ and 39.4 ℃, respectively. The temperature differences remained below 1.0 ℃, indicating negligible PCM influence.

A similar trend was observed for the main switch, whose temperature increased rapidly during the first 15–18 minutes before stabilizing between 43.0 ℃ and 44.0 ℃. The maximum temperature reduction achieved by PCM integration was approximately 1.0 ℃, reflecting the dominance of switching losses and local resistive heating over battery-level thermal buffering.

Connector temperatures were also largely unaffected by PCM configuration, remaining within 40.4–41.2 ℃ throughout the discharge period. These results confirm that connector heating is primarily governed by electrical contact resistance and current flow rather than battery core temperature.

In contrast, the fuse connector consistently exhibited the highest thermal stress. In both no-PCM and beeswax PCM configurations, its temperature rose rapidly and reached 51.0 ℃ by the end of the test. Although lower temperatures were observed in the paraffin PCM case, this deviation was attributed to camera positioning rather than verified thermal improvement. The fuse connector operated 7–11 ℃ hotter than other peripheral components, identifying it as the most critical thermal vulnerability.

3.5 Battery Core Performance

Battery core performance under constant-current operation exhibited measurable differences among thermal management configurations, as summarized in Table 5. The no-PCM battery experienced a voltage drop of

approximately 5.56 V, while beeswax PCM showed a slightly higher drop of 5.88 V. Paraffin PCM exhibited the lowest voltage drop at 4.77 V, indicating improved voltage stability under sustained discharge, consistent with previous findings on thermal buffering effects in lithium-ion batteries [23, 24].

Capacity retention varied across configurations. Beeswax PCM maintained the highest usable capacity, with a 44% reduction, compared to 51% for no PCM and 52% for paraffin PCM. These results demonstrate that while paraffin PCM enhances voltage stability, beeswax PCM provides superior capacity preservation, reflecting differences in thermophysical properties [36, 37].

Battery surface temperature rise was highest without PCM (36.7 ℃) and reduced to 35.5 ℃ and 35.2 ℃ with beeswax and paraffin PCM, respectively. Although the absolute temperature reductions were modest (1.2–1.5 ℃), these reductions contribute to improved electrochemical stability and reduced degradation over repeated cycling [23, 24].

Table 5. Quantitative battery core performance under constant-current discharge (15 A, 30 minutes)

Performance Metric	No PCM	Beeswax PCM	Paraffin PCM	Best Performing Configuration
Voltage drop (V)	5.56	5.88	4.77	Paraffin PCM
Capacity reduction (%)	51	44	52	Beeswax PCM
Final battery temperature (℃)	36.7	35.5	35.2	Paraffin PCM
ΔT vs No (PCM) (℃)	0.0	-1.2	-1.5	Paraffin PCM

3.6 Safety and Design Implications

The thermal data obtained from both variable-load and constant-current experiments provide critical insight for the development of safety strategies and design requirements in high-current electric vehicle power distribution systems. The laboratory-scale tests demonstrated that several interface components reached temperatures approaching levels associated with material degradation. The safety-relevant temperatures and thermal differentials of critical electric vehicle power distribution components are summarized in Table 6.

Table 6. Safety-relevant temperatures and thermal differentials of critical electric vehicle power distribution components

Component/Interface	Operating Condition	Peak Temperature (℃)	ΔT vs Main Switch (℃)	Safety Relevance
Connector	Variable load (>80%)	47.0	+10.5	High
Power cable (+) after main switch	Variable load (>80%)	41.2	+4.7	Moderate–High
Motor cable	Variable load (>80%)	39.7	+3.2	Moderate
Power cable (+) before main switch	Variable load (>80%)	37.4	+0.9	Low–Moderate
Main switch	Variable load (>80%)	36.5	0.0	Reference
Fuse connector	Constant current (15 A, 30 min)	51.0	+14.5	Very High
Battery with phase change material (PCM)	Constant current (15 A, 30 min)	35.2–35.5	-1.0 to -1.3	Low

Thermographic analysis of the cable system revealed that the electrical connector experienced the highest surface temperature, reaching approximately 47.0 ℃ when the system operated at load levels exceeding 80%. Under the same conditions, the power cable located downstream of the main switch reached approximately 41.2 ℃, while the motor cable temperature remained at approximately 39.7 ℃. These values exceeded the temperatures measured at the upstream power cable and the main switch, which reached approximately 37.4 ℃ and 36.5 ℃, respectively. This non-uniform temperature distribution indicates that interface-driven resistive heating concentrates thermal stress within specific regions of the power path rather than producing uniform heating along the conductors. The 10.5 ℃ temperature difference between the connector and the main switch highlights the extent to which electrical interfaces are subjected to localized thermal amplification, which can accelerate insulation aging, promote mechanical degradation, and increase the probability of system failure in high-current applications.

Safety considerations become more pronounced when examining the results of the constant-current PCM experiments. During the 30-minute discharge at 15 A, the fuse connector reached a surface temperature of approximately 51.0 ℃ in both the no-PCM and beeswax PCM configurations. This temperature exceeded those

recorded for the controller (≈40.4 ℃), the main switch (≈44.0 ℃), and standard connectors (≈41.2 ℃) by approximately 7–11 ℃, establishing the fuse connector as the most thermally stressed external component. Operation at these temperature levels has been shown to accelerate polymer degradation, reduce dielectric strength, and increase susceptibility to contact oxidation and loosening, thereby compromising the reliability of protective devices [4].

Integration of PCMs within the battery enclosure reduced battery temperature rise by approximately 1.2–1.5 ℃ and improved voltage stability. However, this intervention did not reduce temperatures at high-resistance interface components. Fuse connector temperatures remained effectively unchanged following PCM integration, indicating that battery-level thermal buffering alone is insufficient to prevent localized overheating at electrical interfaces. The quantitative discrepancy between battery thermal improvement and peripheral component protection reveals a fundamental design limitation associated with reliance on passive, battery-centric thermal management strategies.

These findings indicate that thermal risk mitigation should prioritize interface components rather than bulk conductors. The observed temperature differentials of approximately 5.8 ℃ between the connector and the adjacent power cable, and 3.8 ℃ between downstream and upstream cable segments, demonstrate that localized regions with elevated electrical contact resistance dominate thermal risk. Design strategies aimed at reducing contact resistance through optimized connector geometry, improved conductive materials, enhanced surface treatments, and increased contact pressure that are therefore more effective than uniform increases in cable cross-section or insulation thickness.

The electrical–thermal correlation results further reinforce thee need to integrate thermal safety considerations into electrical system design. Pearson correlation coefficients exceeded 0.89 for all cable and interface components, while voltage ratio exhibited strong negative correlations reaching -0.95. These relationships indicate that electrical operating parameters can serve as early indicators of emerging thermal risk. Real-time monitoring systems that incorporate such parameters enable proactive intervention before surface temperatures reach levels associated with accelerated material degradation.

Overall, the results indicate that future lectric vehicle power distribution systems require interface-focused thermal management solutions to satisfy both safety and design requirements. While passive thermal management strategies enhance battery-level performance, effective mitigation of thermal risk requires targeted protection of connectors, fuse junctions, and post-switch cable segments to ensure long-term system reliability.

The safety discussion presented here is intended as a relative thermal risk assessment rather than a formal compliance evaluation against specific automotive or IEC standards. Although the measured surface temperatures in the range of 47–51 ℃ remain below the absolute failure thresholds for many electrical components, prolonged operation at these levels can accelerate insulation aging, contact oxidation, and mechanical degradation, particularly at electrical interfaces.

International standards such as IEC 60287 and IEC 60364-5-52 provide guidance on current-carrying capacity, permissible conductor temperatures, and derating practices for electrical cables and wiring systems under continuous operation. These standards emphasize conservative thermal margins to limit long-term material degradation rather than catastrophic failure alone. Similarly, connector-related standards applicable to high-current and electric vehicle systems, including IEC 62196 and IEC 60309, implicitly recognize that sustained thermal stress at interfaces necessitates derating and enhanced monitoring to maintain long-term reliability.

Within this framework, the temperature differentials observed in the present study do not indicate immediate non-compliance. Instead, they reveal relative vulnerability zones within the power distribution system. Components such as connectors, fuse junctions, and post-switch cable segments consistently exhibited higher thermal stress than bulk conductors. These findings align with the intent of IEC derating philosophies and underscore the importance of targeted, interface-focused design optimization and condition monitoring to mitigate long-term reliability risks in high-current electric vehicle power systems.

To contextualize the measured temperatures relative to established engineering standards, it is noted that typical insulation materials used in automotive power cables, such as cross-linked polyethylene (XLPE), are commonly rated for continuous operating temperatures of 90–105 ℃, with short-term thermal endurance extending up to approximately 125 ℃ depending on material grade and application (IEC 60228; IEC 60502). Automotive-grade connectors are similarly designed to operate safely at conductor temperatures below approximately 85–105 ℃, with allowable surface temperatures influenced by housing materials, contact design, and ambient conditions.

Accordingly, the peak connector surface temperature observed in this study (approximately 47 ℃) remains well below the absolute thermal limits specified by these standards and does not, by itself, represent an immediate safety violation. The significance of the measured temperatures lies instead in their ability to reveal localized thermal amplification and relative risk concentration at electrical interfaces. Even moderate surface temperatures can accelerate aging mechanisms such as contact oxidation, loss of contact pressure, and insulation degradation, particularly under repeated thermal cycling and prolonged operation. The observed temperatures should therefore be interpreted as relative indicators of thermal vulnerability rather than direct evidence of unsafe operation. The consistent identification of connectors and post-switch cable segments as the hottest regions highlights components where degradation is most likely to initiate over time. In practical electric vehicle systems, where current levels

and duty cycles are substantially higher, these relative thermal patterns may translate into temperatures approaching material limits if not adequately mitigated.

3.7 Model Architecture Neural Network-Based Thermal Prediction Model

A lightweight feedforward ANN was developed to provide accurate thermal prediction while remaining feasible for embedded electric vehicle monitoring. The architecture was selected to balance predictive accuracy with computational efficiency, addressing limitations reported for deeper and more resource-intensive approaches in electric vehicle thermal applications [30, 31]. The key architectural elements are summarized in Table 7.

Table 7. Summary of the artificial neural network (ANN) model architecture

Architectural Element	Quantitative Specification
Network type	Feedforward ANN
Number of input neurons	9
Number of hidden layers	1
Number of hidden neurons	5
Hidden-layer activation	Logistic sigmoid
Number of output neurons	3
Output variables	Main switch, connector, motor cable temperature
Output-layer activation	Linear (identity)
Total trainable parameters	63
Max reported input weight	≈1.036 (power cable after main switch)
Deployment target	Embedded electric vehicle thermal monitoring

To support reproducibility, the training configuration is described as follows. The ANN was trained in a supervised manner, using experimentally measured component temperatures as target outputs. Mean squared error (MSE) was used as the loss function to quantify prediction error during optimization. Network weights and biases were initialized using a random uniform distribution to avoid symmetry and to promote stable convergence.

Training used a gradient-based optimization algorithm with a fixed learning rate of 0.01. The network was trained for 1000 iterations, which was sufficient for convergence given the compact architecture and the limited dataset size. Convergence was confirmed by monitoring stabilization of the training error, with no evidence of divergence or oscillatory behaviour.

Because the experimental dataset was limited, model complexity was constrained to reduce overfitting risk. Robustness was assessed through agreement among ANN predictions, experimental measurements, and benchmark multiple regression results reported in Section 3.8. This design reflects a practical trade-off among transparency, computational cost, and accuracy for embedded electric vehicle thermal monitoring.

The ANN comprised three layers: an input layer with nine neurons, a single hidden layer with five neurons, and an output layer with three neurons. The nine input variables were selected from experimentally measured electrical and thermal parameters that showed meaningful associations with component temperature in the electrical–thermal correlation analysis. The inputs were current, voltage ratio, battery capacity ratio, battery temperature, controller temperature, regulator direct current (DC)–DC temperature, ground cable temperature, power cable temperature before the main switch, and power cable temperature after the main switch. This input set enabled the model to represent both system-level electrical loading and localized thermal conditions.

Nonlinear activation was applied in the hidden layer to represent electro-thermal interactions, including nonlinear relationships between current magnitude and temperature rise, while maintaining numerical stability. Each hidden neuron computed a weighted sum of the nine inputs plus a bias term, followed by a logistic sigmoid transformation. The reported hidden-layer formulation indicates that several coefficients exceeded unity. In particular, battery temperature had weights greater than 1.0 in multiple hidden neurons, and the power cable temperature after the main switch reached a coefficient of 1.036 in one hidden neuron. These weight magnitudes indicate that the learned representation was strongly influenced by downstream cable heating and battery thermal state, consistent with experimentally observed vulnerability patterns.

The output layer contained three neurons that predicted main switch temperature, connector temperature, and motor cable temperature. A linear (identity) activation function was applied at the output layer to preserve the continuous nature of temperature outputs. Predicted temperatures were computed as weighted linear combinations of hidden-layer activations with bias terms. The reported coefficients indicate that all five hidden neurons contributed to the outputs, suggesting that prediction was not dominated by a single hidden unit and that the network distributed learned electro-thermal relationships across the hidden representation.

The network contained 63 trainable parameters. This total comprised 45 input-to-hidden weights (9 × 5), five hidden-layer biases, 15 hidden-to-output weights (5 × 3), and three output biases. This parameter count is substantially lower than that of many deep learning architectures for electric vehicle thermal prediction, which often involve hundreds to thousands of parameters. The compact parameterization reduces memory requirements and computational overhead, supporting deployment on low-power embedded controllers.

The forward-pass computation required only basic arithmetic operations and evaluation of the sigmoid function, enabling rapid temperature estimation without dedicated hardware accelerators. The resulting balance between model size and representational capacity supports the observed predictive performance and indicates that higher-complexity deep architectures are not necessarily required to capture dominant electro-thermal behaviour in the investigated electric vehicle power cable system.

The detail of the algorithm can be shown as follows:

1. Activation Function

The logistic sigmoid activation function is defined as:

$$f(z) = \frac{1}{1 + e^{-z}} \tag{1}$$

2. Hidden Layer 5 Neurons (Activation: Logistic Sigmoid)

Hidden Neuron h_1

$$\begin{aligned} z_1 = & -0.578\,\mathrm{V\_ratio} - 0.389\,\mathrm{I} - 1.031\,\mathrm{Battery\_capacity\_ratio} \\ & + 0.036\,\mathrm{Controller\_Temp} + 1.056\,\mathrm{Battery\_Temp} + 0.791\,\mathrm{Regulator\_Temp} \\ & + 0.489\,\mathrm{Ground\_Cable\_Temp} + 0.392\,\mathrm{PowerCable\_Before\_Temp} \\ & + 0.286\,\mathrm{PowerCable\_After\_Temp} - 1.031 \end{aligned} \tag{2}$$

$$h_1 = f\left(z_1\right) \tag{3}$$

Hidden Neuron h_2

$$\begin{aligned} z_2 = & -0.326\,\mathrm{V\_ratio} - 0.166\,\mathrm{I} + 0.089\,\mathrm{Battery\_capacity\_ratio} \\ & + 0.062\,\mathrm{Controller\_Temp} + 0.396\,\mathrm{Battery\_Temp} + 0.099\,\mathrm{Regulator\_Temp} \\ & + 0.186\,\mathrm{Ground\_Cable\_Temp} + 0.325\,\mathrm{PowerCable\_Before\_Temp} \\ & + 0.572\,\mathrm{PowerCable\_After\_Temp} - 0.194 \end{aligned} \tag{4}$$

$$h_2 = f\left(z_2\right) \tag{5}$$

Hidden Neuron h_3

$$\begin{aligned} z_3 = & -0.041\,\mathrm{V\_ratio} + 0.370\,\mathrm{I} - 0.425\,\mathrm{Battery\_capacity\_ratio} \\ & + 0.705\,\mathrm{Controller\_Temp} + 1.068\,\mathrm{Battery\_Temp} + 0.657\,\mathrm{Regulator\_Temp} \\ & + 0.144\,\mathrm{Ground\_Cable\_Temp} + 0.056\,\mathrm{PowerCable\_Before\_Temp} \\ & + 0.028\,\mathrm{PowerCable\_After\_Temp} + 0.004 \end{aligned} \tag{6}$$

$$h_3 = f\left(z_3\right) \tag{7}$$

Hidden Neuron h_4

$$\begin{aligned} z_4 = & -0.611\,\mathrm{V\_ratio} + 0.109\,\mathrm{I} - 0.109\,\mathrm{Battery\_capacity\_ratio} \\ & + 0.139\,\mathrm{Controller\_Temp} + 0.163\,\mathrm{Battery\_Temp} + 0.215\,\mathrm{Regulator\_Temp} \\ & + 0.485\,\mathrm{Ground\_Cable\_Temp} + 0.626\,\mathrm{PowerCable\_Before\_Temp} \\ & + 0.738\,\mathrm{PowerCable\_After\_Temp} - 0.116 \end{aligned} \tag{8}$$

$$h_4 = f(z_4) \tag{9}$$

Hidden Neuron h_5

$$\begin{aligned} z_5 = & -1.655\,\mathrm{V\_ratio} - 0.875\,\mathrm{I} + 0.229\,\mathrm{Battery\_capacity\_ratio} \\ & - 0.338\,\mathrm{Controller\_Temp} - 0.485\,\mathrm{Battery\_Temp} + 0.582\,\mathrm{Regulator\_Temp} \\ & + 0.591\,\mathrm{Ground\_Cable\_Temp} + 0.851\,\mathrm{PowerCable\_Before\_Temp} \\ & + 1.036\,\mathrm{PowerCable\_After\_Temp} - 1.385 \end{aligned} \tag{10}$$

$$h_5 = f(z_5) \tag{11}$$

3. Output Layer 3 Neurons (Activation: Identity)

$$\text{Main Switch Temp} = 0.781h_1 + 0.686h_2 - 0.032h_3 + 0.017h_4 + 0.392h_5 - 0.340 \tag{12}$$

$$\text{Connector Temp} = -0.844h_1 + 0.836h_2 - 0.403h_3 + 0.976h_4 + 1.941h_5 - 0.504 \tag{13}$$

$$\text{Motor Cable Temp} = 0.587h_1 + 0.248h_20.779h_3 - 0.405h_4 + 0.664h_5 - 0.365 \tag{14}$$

3.8 Training and Validation Model Artificial Neural Network (ANN)

The dataset was randomly divided into 70% for training and 30% for testing. Model performance was evaluated using the coefficient of determination (R^2), mean absolute error (MAE), and root mean square error (RMSE), calculated exclusively on the unseen test set. No hyperparameter tuning or model adjustment was conducted using the test data to avoid optimistic bias and to support an unbiased assessment of generalization performance.

Predictive performance was first evaluated using parity plots that compare experimentally measured temperatures and ANN-predicted values for the main switch, connector, and motor cable, as shown in Figure 7. The parity plots show a strong linear agreement between predicted and measured values, with most points clustered near the identity line ($y = x$). This agreement indicates that the ANN captured the dominant electro-thermal relationships governing system behaviour [30, 31].

For the main switch, Figure 7a shows excellent predictive accuracy, with R^2 = 0.9938 and low error values (MAE = 0.138 ℃, RMSE = 0.204 ℃). The tight clustering of points around the identity line is consistent with the relatively stable thermal behaviour of the main switch under the investigated operating conditions, where heat generation is dominated by predictable resistive losses [30]. For the connector, Figure 7b shows similarly strong agreement, with R^2 = 0.9854. The associated errors were higher than for the main switch (MAE = 0.402 ℃, RMSE = 0.667 ℃), which is consistent with greater thermal variability caused by contact resistance fluctuations and load-dependent interface effects [31]. For the motor cable, Figure 7c shows a clear linear trend with R^2 = 0.9007. The corresponding MAE and RMSE values (0.400 ℃ and 0.812 ℃) were higher than those of the other components, reflecting more dynamic behaviour associated with spatially distributed heating and convective effects. However, the absence of systematic deviation from the identity line indicates that the ANN maintained acceptable generalization across the examined temperature range [31].

To benchmark the ANN against a simpler predictive method, multiple linear regression (MLR) models were evaluated using the same dataset. Unlike the ANN, which used a single unified model to predict main switch, connector, and motor cable temperatures simultaneously, MLR required three independent component-specific models. The MLR models achieved high accuracy, with R^2 values of 0.9936, 0.9991, and 0.9961 for the main switch, connector, and motor cable, respectively, and correspondingly low MAE and RMSE values, as reported in Table 8.

Although the MLR models yielded slightly lower error metrics in some cases, their structure remained component-specific and did not provide a unified representation of coupled electro-thermal interactions. In contrast, the ANN achieved comparable accuracy using a single compact model trained on 14 operating points, while also representing multi-component coupling within the power distribution system.

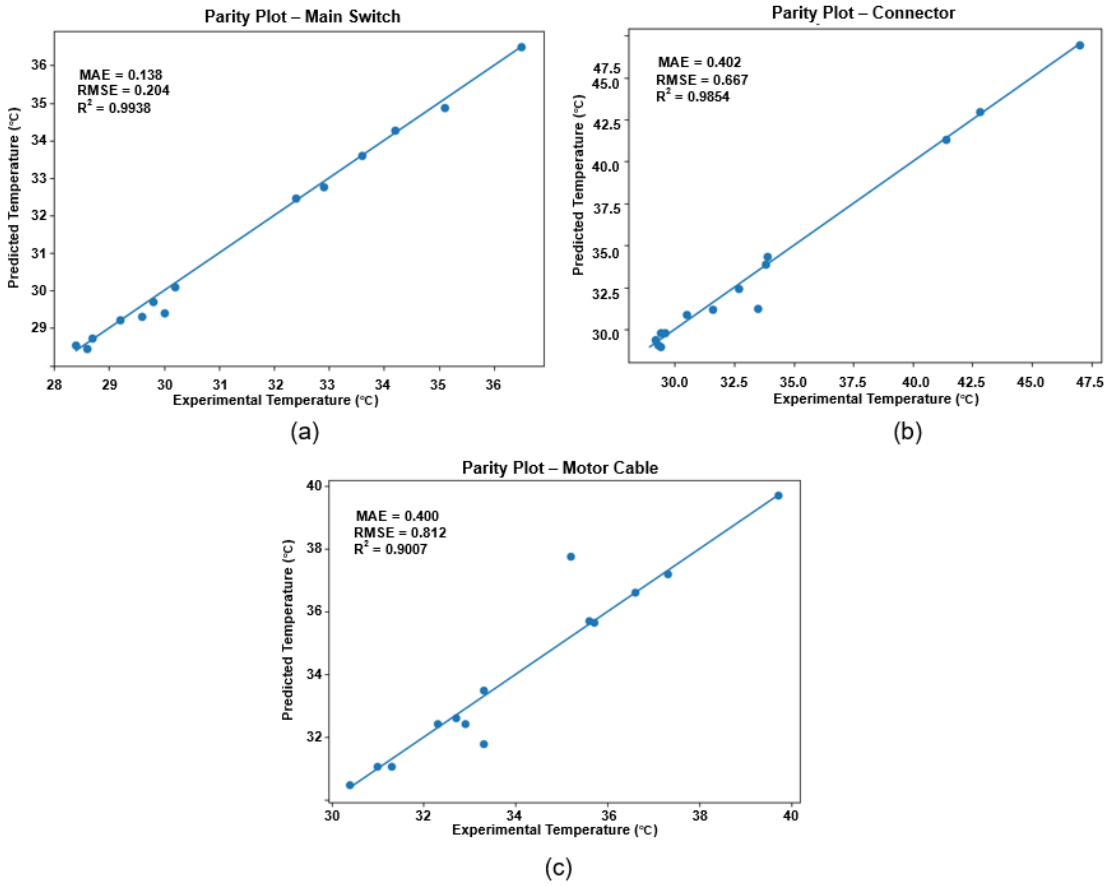

Figure 7. Parity plots comparing experimentally measured and ANN-predicted temperatures for (a) main switch; (b) connector; (c) motor cable. The solid line represents the identity line ($y = x$). The analysis is based on $n = 14$ samples, including both training and testing data. Temperatures are expressed in degrees Celsius (°C)

Table 8. Benchmarking of multiple linear regression (MLR)

Model	R^2	Mean Absolute Error (MAE) (°C)	Root Mean Square Error (RMSE) (°C)
Main switch	0.9936	0.155	0.206
Connector	0.9991	0.068	0.079
Motor cable	0.9961	0.287	0.346

This unified modelling approach reduces deployment complexity in practical electric vehicle applications, where maintaining separate models for each component increases calibration effort and system management burden [36]. Given the limited dataset, the ANN was intentionally kept lightweight to reduce overfitting risk. The close agreement between ANN predictions, experimental measurements, and MLR benchmarks supports the robustness of the proposed model. The ANN should therefore be interpreted as a proof-of-concept framework that balances accuracy, computational efficiency, and system-level integration, rather than as a universally transferable model for all electric vehicle configurations [30, 37].

Although the parity analysis indicates strong predictive performance, correlation-based evaluation alone does not fully characterize agreement. Therefore, Bland–Altman analysis was used to assess systematic bias and limits of agreement, as shown in Figure 8, based on $n = 14$ paired samples for each component. The Bland–Altman method plots the difference between predicted and measured temperatures against their mean, with limits of agreement defined as ±1.96 standard deviations (SD) from the mean difference, corresponding to a 95% confidence interval.

For the main switch, Figure 8a shows a mean difference of -0.089 °C, indicating negligible systematic bias. All data points fell within the ±1.96 SD limits, suggesting that prediction errors were bounded and randomly distributed. This agreement is consistent with the low MAE and RMSE values obtained from the parity analysis. For the connector, Figure 8b shows a mean difference of -0.138 °C and wider limits of agreement, consistent with the higher dispersion and error values observed in Figure 7b. Nevertheless, most observations remained within the agreement

bounds, supporting reliable predictive performance under increased interface-driven variability. For the motor cable, Figure 8c shows a small positive mean difference of +0.055 ℃, indicating a slight tendency toward overprediction. However, no proportional bias or temperature-dependent trend was observed, and all points fell within the defined limits of agreement, indicating stable performance despite more dynamic thermal behaviour.

Taken together, the parity and Bland–Altman analyses indicate that the ANN produced accurate and largely unbiased predictions for all three components. The bounded error ranges and absence of systematic bias support its suitability for thermal monitoring and predictive analysis in complex electrical systems.

Given the limited dataset size (n = 14 operating points), the validation strategy was designed to balance predictive reliability, model transparency, and overfitting mitigation. The dataset was divided into a training subset (70%, n = 10) and a testing subset (30%, n = 4). Training data were used exclusively for weight optimization, and the test subset was reserved for post-training evaluation. Formal k-fold cross-validation was not applied because the small sample size would reduce effective training samples per fold and increase variance in estimated performance. Instead, overfitting risk was controlled through architectural constraint and benchmarking. The ANN used one hidden layer with five hidden neurons, resulting in 63 trainable parameters, which limited model capacity and reduced the likelihood of memorizing noise.

Model convergence was monitored through stabilization of the training loss (MSE). Training was terminated after 1000 iterations once the loss plateaued, and no oscillatory or divergent behaviour was observed. Benchmarking against MLR models provided additional evidence that the ANN did not overfit the data, as both approaches produced close agreement with experimental observations. On the test set, the ANN achieved MAE values below 0.5 ℃ and RMSE values below 1.0 ℃ for all three predicted components. These errors remain within the uncertainty range of infrared thermography measurements (±2 ℃), supporting acceptable generalization performance on unseen operating points.

The ANN is intended as an operational thermal estimator tailored to the investigated electric vehicle power distribution configuration rather than a universally transferable model. The objective is to provide a lightweight, interpretable, and computationally efficient predictor for embedded monitoring and early thermal risk detection. Transfer to other electric vehicle architectures would require retraining using configuration-specific experimental data.

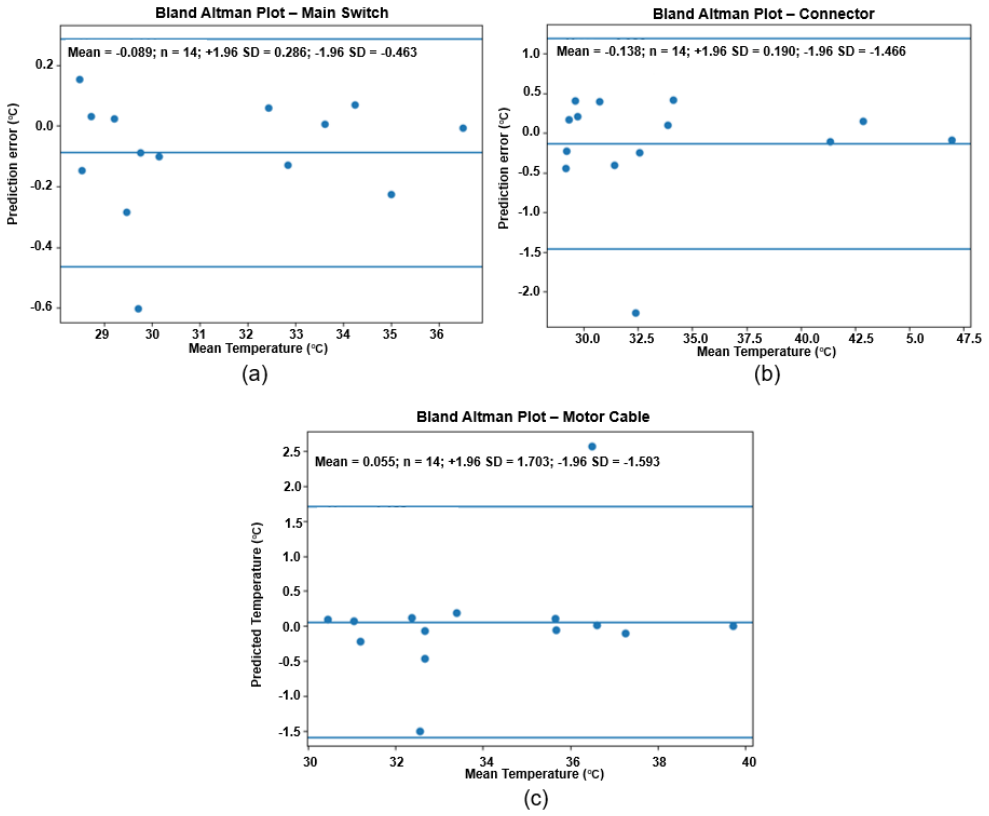

Figure 8. Bland–Altman plots illustrating the agreement between ANN-predicted and experimentally measured temperatures for (a) main switch; (b) connector; (c) motor cable (n = 14). The central line indicates the mean difference, while the upper and lower lines represent the 95% limits of agreement (±1.96 standard deviations). All temperature values are expressed in degrees Celsius (℃)

3.9 Feature Model ANN Contribution Analysis

The correlation analysis in Section 3.3 served two functions. First, it provided an interpretable overview of which electrical indicators were most strongly associated with thermal stress. Second, it informed input selection for the ANN by prioritizing variables with consistent and physically meaningful associations with temperature, including current, voltage ratio, battery capacity ratio, and representative thermal-state variables. Building on this screening, feature contribution analysis was conducted to examine whether the ANN relied on physically plausible drivers rather than arbitrary patterns, which is particularly important given the limited dataset.

Feature contribution was inferred from normalized absolute weights linking input neurons to the hidden layer and subsequently to the output layer. This approach provided a quantitative proxy for the relative influence of each input variable on predicted temperatures.

Battery temperature was the most influential input across all outputs, contributing approximately 22–25% of the total normalized weight magnitude. This dominance indicates strong coupling between battery thermal state and downstream component temperatures during sustained current operation. The result is consistent with the correlation trends reported in Section 3.3 and with prior studies indicating that elevated battery temperature increases resistive losses in the power distribution system [18, 28].

The power cable temperature after the main switch was the second most influential feature, contributing approximately 18–21% of total weight magnitude. This finding supports the experimental observation that downstream cable segments exhibit elevated thermal stress relative to upstream sections. The strong contribution of this feature indicates that post-switch heating is a useful predictor of temperature escalation in adjacent interfaces, including connectors and motor cables.

Electrical current contributed approximately 15–18% of total feature influence, reinforcing its role in resistive heating. Although current was not the largest contributor, its influence remained substantial, reflecting the nonlinear interaction between electrical loading and localized thermal accumulation. The model therefore integrated both global electrical stress indicators and local thermal state variables rather than relying on a single dominant input.

Voltage ratio and battery capacity ratio provided moderate contributions, accounting for approximately 8–11% and 7–10% of total influence, respectively. These variables represent indirect stress indicators through voltage sag and state-of-charge-related effects and are consistent with the negative associations identified in Section 3.3. Although they are not primary determinants of temperature rise on their own, their inclusion strengthens predictive robustness by contextualizing current-driven heating under broader operating conditions.

Lower contributions were observed for controller temperature, regulator DC–DC temperature, and ground cable temperature, each contributing less than 7% individually. These features provided supplementary thermal context but did not dominate prediction of main switch, connector, or motor cable temperature. This pattern supports the interpretation that thermal risk is primarily driven by battery state and interface-adjacent conductors rather than upstream electronics.

The contribution profile remained broadly consistent across the three predicted outputs, indicating that no single input exclusively controlled any output. This distributed representation improves model stability and reduces sensitivity to noise in any single measurement channel. Importantly, the feature ranking aligns with physical expectations and with experimental observations, addressing interpretability concerns in safety-relevant modelling contexts [31, 38]. Compared with deeper architectures, the lightweight ANN preserves clearer mapping between physical parameters and predicted temperatures. The feature contribution results are reported in Table 9.

Table 9. Feature contribution to artificial neural network (ANN) temperature prediction

Input Feature	Contribution (%)	Relative Importance
Battery temperature	22–25	Very High
Power cable temperature after main switch	18–21	High
Electrical current	15–18	High
Voltage ratio	8–11	Moderate
Battery capacity ratio	7–10	Moderate
Controller temperature	5–7	Low–Moderate
Regulator direct current (DC)–DC temperature	4–6	Low
Ground cable temperature	3–5	Low

4 Discussion

All temperature measurements in this study were obtained using infrared thermography, which captures surface temperatures of cables, connectors, and electrical components. Internal conductor and contact temperatures can exceed surface measurements because of thermal gradients across insulation layers and limited internal heat

dissipation. The reported values should therefore be interpreted as conservative lower-bound estimates of internal thermal stress. Infrared thermography also introduces inherent uncertainty related to emissivity settings, surface reflectivity, camera viewing angle, and intrinsic camera accuracy (±2 ℃). These factors may influence absolute temperature values. However, they do not affect the relative temperature hierarchy or hotspot localization, both of which remained consistent across repeated operating conditions. Therefore, the comparative thermal ranking and hotspot identification reported here are considered robust.

The experimental scenarios included stepwise load increases and constant-current operation. These conditions were controlled and repeatable, which made them suitable for evaluating cumulative thermal stress and steady-state hotspot formation. Real electric vehicle operation also involves transient events such as rapid acceleration, regenerative braking, and fast-charging initiation. These short-duration current fluctuations were not examined in the present work. Instead, this study focused on sustained thermal exposure because it governs insulation aging, contact degradation, and long-term reliability. Accordingly, the proposed diagnostic and predictive framework is intended for continuous thermal monitoring rather than instantaneous transient peak capture. Dynamic operating conditions are therefore identified as a priority for future investigation.

The current levels investigated in this study are lower than those typically encountered in commercial fast-charging electric vehicles. For this reason, the results should not be interpreted as direct predictors of absolute temperature levels in full-scale electric vehicle systems. The findings are primarily valid for relative hotspot identification, thermal vulnerability ranking, and comparative electro-thermal behaviour among power distribution components under increasing electrical load.

The observed temperature hierarchy, particularly the persistent dominance of connectors and post-switch cable segments as hotspots, reflects interface-driven resistive heating. This behaviour is governed mainly by contact resistance, geometry, and local heat dissipation conditions rather than by current magnitude alone. As a result, absolute temperatures are scale-dependent. In contrast, relative trends and hotspot locations remain physically meaningful within the tested configuration.

Transferability to higher-current electric vehicle platforms is expected when connector geometry, contact materials, assembly pressure, and cooling boundary conditions are comparable to those investigated here. Under these similarities, increased current would primarily amplify temperature rise magnitude without fundamentally changing the spatial distribution of thermal stress. The experimental framework and analytical approach therefore provide a basis for comparative thermal diagnostics and early-stage design evaluation rather than direct absolute temperature prediction for full-scale electric vehicle applications. The temperature values should be interpreted as relative indicators obtained from a scaled experimental platform. Direct transfer of absolute temperature levels to high-current commercial systems requires further validation under comparable conductor cross-sections, connector geometries, material properties, and cooling boundary conditions.

The purpose of this study is not to define absolute temperature limits at a specific current magnitude. Instead, it is to identify which components in the electric vehicle power distribution system are most thermally critical during motor operation. In this context, current acts as an excitation mechanism that activates electro-thermal processes rather than as a scaling parameter for absolute temperature prediction. Resistive heating occurs throughout conductive paths when current flows. However, the distribution of thermal stress is governed by intrinsic factors, including contact resistance, interface geometry, material discontinuities, and heat dissipation capability. These characteristics are inherent to the system architecture and do not change with current magnitude. Therefore, although higher currents raise overall temperatures, the identity and ranking of thermally critical components are expected to remain stable.

The thermographic results in Figure 5 illustrate this behaviour. Under no-load conditions, all monitored components operated below 30 ℃, which indicates minimal resistive heating. At moderate load (40–60%), connector temperature increased more rapidly than adjacent components and reached approximately 38 ℃, while cable segments remained at or below 37 ℃. This behaviour represents the first clear separation caused by interface losses. At load levels exceeding 80%, the connector reached 47.0 ℃. In contrast, cable segments remained below 41.2 ℃. The main switch housing showed the lowest temperature (36.5 ℃). The pre-switch cable reached 37.4 ℃, the motor cable reached 39.7 ℃, and the post-switch cable reached 41.2 ℃. This hierarchy was reproduced across load-increment tests (Table 3) and agrees with prior studies identifying connectors and junctions as dominant thermal barriers in high-current electric vehicle systems [1, 2, 19]. For reference, the peak connector temperature of approximately 47 ℃ remains well below typical automotive power cable and connector ratings, which are commonly in the range of 90–105 ℃ for continuous operation. This indicates that the present setup represents an early-stage thermal risk scenario rather than an immediate safety violation.

Additional evidence of interface-driven thermal amplification was observed across the main switch. Although the same current flowed through both segments, the downstream power cable operated approximately 3.8 ℃ hotter than the upstream section. This indicates that switching interfaces introduce additional resistance and transition losses that propagate into adjacent conductors [14, 15]. The connector showed stronger amplification. It operated 5.8 ℃ above

the post-switch cable and 10.5 ℃ above the main switch (Table 2). This localized overheating is critical because interface temperature rise accelerates insulation degradation, contact oxidation, and mechanical deterioration more rapidly than distributed cable heating [10, 11].

The electrical–thermal correlation results in Figure 6 provide quantitative support for these observations. All components showed positive correlations between current and temperature (r = 0.628–0.946). The controller exhibited the strongest association (r = 0.946), followed by the pre-switch cable (r = 0.910), ground cable (r = 0.900), and DC–DC regulator (r = 0.892). These relationships align with Joule heating behaviour, where temperature rise increases with current magnitude. Voltage ratio showed consistently negative correlations (r = -0.563 to -0.952) for cables and the connector. This suggests increased resistive losses and higher thermal stress during voltage sag conditions [3, 7]. Battery capacity ratio also showed negative correlations with temperature, particularly for the main switch (r = -0.846), DC–DC regulator (r = -0.826), and battery (r = -0.825). This pattern is consistent with increased internal resistance during extended operation, which elevates thermal stress [18, 28]. In contrast, the connector showed weak correlation with battery state, which indicates that its thermal behaviour is primarily governed by current flow and local contact resistance rather than battery condition.

The PCM experiments highlight limitations of battery-focused passive thermal management. PCM integration reduced battery temperature rise by approximately 1.2–1.5 ℃ and improved voltage stability. However, peripheral component temperatures differed by less than 1.0 ℃ from baseline values (Table 3 and Table 4). Under constant-current operation, the fuse connector reached 51.0 ℃ and exceeded other peripheral components by 7–11 ℃ (Table 5). These results indicate that PCMs can improve battery-level performance but do not mitigate localized interface heating driven by high resistance. This outcome is consistent with reported limitations of passive thermal management in addressing interface-dominated hotspots [23, 24]. Operation of protective junctions near 50 ℃ may accelerate material degradation and reduce reliability, which reinforces the need for interface-specific mitigation strategies [4].

Finally, the ANN results support the experimental findings and demonstrate that a compact predictive model grounded in physically meaningful inputs can predict component temperatures with high accuracy using limited data. Using 14 operating points, the ANN achieved R^2 values of 0.9938 for the main switch, 0.9854 for the connector, and 0.9007 for the motor cable. The MAE and RMSE values remained within standard thermographic uncertainty limits. Bland–Altman analysis indicated minimal systematic bias (-0.15 ℃ to +0.15 ℃) across components. Feature contribution analysis further supported physical consistency by identifying battery temperature, post-switch cable temperature, and current as dominant predictors, consistent with observed hotspot patterns. The lightweight ANN therefore provides a transparent and computationally efficient alternative to deep learning approaches, supporting its suitability for embedded electric vehicle thermal monitoring under limited data and processing resources [30, 31].

5 Conclusions

This study presents an integrated experimental and computational assessment of electro-thermal behaviour in an electric vehicle power distribution system, with the objective of identifying thermally critical components and evaluating mitigation and prediction strategies. The results show that thermal stress within the power distribution path is primarily governed by interface-driven heating rather than uniform conductor heating. Electrical connectors and protective junctions consistently emerge as the dominant hotspots under both variable-load and constant-current conditions, highlighting the critical role of contact resistance in thermal risk development.

The investigation of PCM integration demonstrates that battery-level passive thermal management improves battery temperature stability and voltage behaviour but has negligible impact on the thermal response of peripheral power distribution components. This finding reveals a system-level limitation of battery-focused thermal solutions and underscores the need for interface-specific design and protection strategies.

Electrical-thermal correlation analysis indicates that current magnitude, voltage ratio, and battery condition serve as effective diagnostic indicators of thermal stress. These parameters provide a practical basis for condition monitoring and early detection of emerging hotspots in electric vehicle power systems. Finally, a lightweight ANN model is shown to deliver accurate and unbiased temperature predictions for multiple critical components using a single unified model, despite the limited experimental dataset. Compared with MLR, the ANN offers comparable accuracy while providing improved system-level integration and suitability for embedded monitoring. Overall, the study emphasizes that reliable electric vehicle thermal management requires interface-focused mitigation combined with compact predictive tools rather than battery-level solutions alone.

Author Contributions

Conceptualization, S.G.H; methodology, S.G.H. and A.N.F.S.; validation, S.G.H. and S.Y.; formal analysis, S.G.H. and S.Y.; investigation, S.Y. and B.P.Y.; resources, A.N.F.S., S.Y., and B.P.Y.; data curation, S.G.H. and S.Y.; writing—original draft preparation, S.G.H. and S.Y.; writing—review and editing, S.G.H. and A.N.F.S.;

visualization, S.G.H. and B.P.Y.; supervision, S,G.H.; project administration, A.N.F.S. All authors were actively involved in discussing the findings and refining the final manuscript.

Data Availability

All the datasets used in this study are available from the Zenodo database.
Accession number: https://zenodo.org/records/16614762.

Conflicts of Interest

The authors declare that they have no conflicts of interest.

References

[1] S. G. Hwang, M. Lee, and B. D. Ko, "Numerical analysis on cooling performances for connectors using immersion cooling in ultra-fast chargers for electric vehicles," *Symmetry*, vol. 17, no. 4, p. 624, 2025. https://doi.org/10.3390/sym17040624

[2] U. Musa, A. A. Mati, A. A. Mas'ud, G. S. Shehu, S. H. Sulaiman, and J. M. Rodríguez-Serna, "Investigation of electric field enhancement and effects of discharge severity in an insulated power cable with multiple gaseous cavities," *Niger. J. Technol. Dev.*, vol. 20, no. 3, pp. 142–153, 2023. https://doi.org/10.4314/njtd.v20i3.1435

[3] K. Emdadi, "Overview of monitoring, diagnostics, aging analysis, and maintenance strategies in high-voltage AC/DC XLPE cable systems," *Sensors*, vol. 25, no. 22, p. 7096, 2025. https://doi.org/10.3390/s25227096

[4] N. B. Mehta and P. R. Patel, "The advancement in battery with composition of lithium-titanium oxide (Lto) in electric vehicles," *Int. J. Environ. Sci.*, vol. 11, no. 21s, pp. 4294–4306, 2025. https://doi.org/10.64252/3ypz1q39

[5] G. Town, S. Taghizadeh, and S. Deilami, "Review of fast charging for electrified transport: Demand, technology, systems, and planning," *Energies*, vol. 15, no. 4, p. 1276, 2022. https://doi.org/10.3390/en15041276

[6] E. Kantar, K. K. Eie-Klusmeier, T. A. Ve, M. Ese, and S. Hvidsten, "Electrical aging of fluoropolymer cable insulation materials induced by partial discharge," *IEEE Trans. Dielectr. Electr. Insul.*, vol. 32, no. 1, pp. 416–427, 2025. https://doi.org/10.1109/tdei.2024.3402663

[7] Y. Li, G. Zhen, Y. Liu, H. Song, Y. Liang, X. Liu, S. Meng, Y. Liu, and S. Li, "Effect of temperature on partial discharges activity and electrical trees propagation in XLPE," *IET Sci. Meas. Technol.*, vol. 18, no. 6, pp. 300–309, 2024. https://doi.org/10.1049/smt2.12199

[8] P. K. Nema, Vijaya, P. Muthukumar, and R. Thangavel, "Recent advancements and future prospects in lithium-ion battery thermal management techniques," *Energy Storage*, vol. 6, no. 8, p. e70076, 2024. https://doi.org/10.1002/est2.70076

[9] P. Panmuang, C. Photong, and C. Soemphol, "Experimental investigation of batteries thermal management system using water cooling and thermoelectric cooling techniques," *Int. J. Power Electron. Drive Syst.*, vol. 15, no. 1, p. 201, 2024. https://doi.org/10.11591/ijpeds.v15.i1.pp201-212

[10] J. A. Martinez, J. Riba, and M. Moreno-Eguilaz, "State of health prediction of power connectors by analyzing the degradation trajectory of the electrical resistance," *Electronics*, vol. 10, no. 12, p. 1409, 2021. https://doi.org/10.3390/electronics10121409

[11] A. Gómez-Pau, J. Riba, and M. Moreno-Eguilaz, "Time series rul estimation of medium voltage connectors to ease predictive maintenance plans," *Appl. Sci.*, vol. 10, no. 24, p. 9041, 2020. https://doi.org/10.3390/app10249041

[12] B. Wen, J. Pan, P. Qian, L. Zhang, W. Chen, and J. Zhang, "Research on the influence of the closing amount of electrical connector contacts on fretting wear under a vibration environment," *Electronics*, vol. 12, no. 11, p. 2469, 2023. https://doi.org/10.3390/electronics12112469

[13] J. Ni, L. Han, J. Pan, J. Zheng, Y. Shi, Z. Cui, and J. Cai, "Evolution of contact performance of industry electrical connector based on reliability accelerated testing," *Adv. Mech. Eng.*, vol. 13, no. 2, pp. 1–12, 2021. https://doi.org/10.1177/1687814021998829

[14] J. Riba, A. Gómez-Pau, J. A. Martinez, and M. Moreno-Eguilaz, "On-line remaining useful life estimation of power connectors focused on predictive maintenance," *Sensors*, vol. 21, no. 11, p. 3739, 2021. https://doi.org/10.3390/s21113739

[15] R. Rohith, S. Shivakumar, S. J. Niranjana, V. Umesh, S. M. Darshan, and J. Sasidhar, "Design optimization of electrical connector assembly using FEA," *J. Mines Met. Fuels*, vol. 70, no. 8A, pp. 233–237, 2022. https://doi.org/10.18311/jmmf/2022/31981

[16] S. Y. Sayenko, K. P. Msallam, T. K. Muradyan, and N. B. Perekhrest, "Computer-aided design of innovative liquid cooling systems for cables in electric vehicle charging stations: Analysis and prospects," *Open Inf. Comput. Integr. Technol.*, no. 103, pp. 37–45, 2025. https://doi.org/10.32620/oikit.2025.103.03

[17] Q. Hu, M. R. Amini, I. Kolmanovsky, J. Sun, A. Wiese, and J. B. Seeds, "Multihorizon model predictive control: An application to integrated power and thermal management of connected hybrid electric vehicles," *IEEE Trans. Control Syst. Technol.*, vol. 30, no. 3, pp. 1052–1064, 2022. https://doi.org/10.1109/tcst.2021.3091887

[18] T. Wu, K. T. Cheng, J. Kang, and R. Liu, "Remaining useful life prediction of lithium-ion batteries based on a combination of ensemble empirical mode decomposition and deep belief network–long short-term memory," *Energy Technol.*, vol. 12, no. 5, p. 2301033, 2024. https://doi.org/10.1002/ente.202301033

[19] E. Trancho, E. Ibarra, P. Prieto, A. Arias, A. Lis, and A. P. Pai, "Novel thermal management strategy for improved inverter reliability in electric vehicles," *Appl. Sci.*, vol. 10, no. 22, p. 8024, 2020. https://doi.org/10.3390/app10228024

[20] H. O. Njoku, E. Onah, M. S. Torbira, and O. A. Egonu, "Condition assessment of electrical power devices using infrared thermography: A review," *ASM Sci. J.*, vol. 19, pp. 1–19, 2024. https://doi.org/10.32802/asmscj.2023.549

[21] A. Mahami, C. Rahmoune, T. Bettahar, and D. Benazzouz, "Induction motor condition monitoring using infrared thermography imaging and ensemble learning techniques," *Adv. Mech. Eng.*, vol. 13, no. 11, pp. 1–13, 2021. https://doi.org/10.1177/16878140211060956

[22] Y. Chung, S. Lee, and W. Kim, "Latest advances in common signal processing of pulsed thermography for enhanced detectability: A review," *Appl. Sci.*, vol. 11, no. 24, p. 12168, 2021. https://doi.org/10.3390/app112412168

[23] G. Mao and J. Jiang, "Preparation and application of composite phase change materials," *Adv. Comput. Eng. Technol. Res.*, vol. 1, no. 2, p. 558, 2024. https://doi.org/10.61935/acetr.2.1.2024.p558

[24] M. J. Quarrell, R. Batty, A. R. Neale, D. Harvey, D. G. Shchukin, and L. J. Hardwick, "Integration of micro-encapsulated phase change materials into thin coatings for a passive battery thermal management system," *ECS Meet. Abstr.*, vol. MA2025-01, no. 8, pp. 835–835, 2025. https://doi.org/10.1149/ma2025-018835mtgabs

[25] W. Fu and J. Gao, "Research on robot thermal management technology based on composite phase change material," *J. Phys. Conf. Ser.*, vol. 3068, no. 1, p. 012139, 2025. https://doi.org/10.1088/1742-6596/3068/1/012139

[26] J. Wang, M. O. H. Schutzeichel, B. Plaumann, T. Kletschkowski, and A. Panesar, "Multidisciplinary design optimisation of lattice-based battery housing for electric vehicles," *Sci. Rep.*, vol. 14, no. 1, pp. 1–14, 2024. https://doi.org/10.1038/s41598-024-60124-4

[27] C. Y. Guo, M. W. Muhieldeen, K. H. Teng, and A. Show, "A critical review of advancements and challenges in thermal management systems for lithium-ion batteries," *J. Adv. Res. Numer. Heat Transf.*, vol. 35, no. 1, pp. 117–161, 2025. https://doi.org/10.37934/arnht.35.1.117161

[28] Z. Xing, W. Ding, S. Zhang, L. Zhong, L. Wang, J. Wang, K. Wang, Y. Xie, X. Zhao, N. Li, and Z. Ye, "Machine learning-based differentiation of nontuberculous mycobacteria lung disease and pulmonary tuberculosis using CT images," *Biomed. Res. Int.*, vol. 2020, p. 6287545, 2020. https://doi.org/10.1155/2020/6287545

[29] G. Liu, L. Kui, Y. Gao, W. Cui, F. Liu, and W. Wang, "Machine learning-based optimization of synchronous rectification low-inductance current secondary boost converter (SLIC-QBC)," *Energies*, vol. 16, no. 18, p. 6690, 2023. https://doi.org/10.3390/en16186690

[30] T. Guillod, P. Papamanolis, and J. W. Kolar, "Artificial neural network (ANN) based fast and accurate inductor modeling and design," *IEEE Open J. Power Electron.*, vol. 1, pp. 284–299, 2020. https://doi.org/10.1109/ojpel.2020.3012777

[31] I. A. Doush, M. A. Awadallah, M. A. Al-Betar, O. A. Alomari, S. N. Makhadmeh, A. K. Abasi, and Z. A. A. Alyasseri, "Archive-based coronavirus herd immunity algorithm for optimizing weights in neural networks," *Neural Comput. Appl.*, vol. 35, pp. 15 923–15 941, 2023. https://doi.org/10.1007/s00521-023-08577-y

[32] O. Yatskiv and B. Koman, "Assessing the potential of artificial intelligence and machine learning for thermal management in electronic devices," *Technol. Audit Prod. Reserv.*, vol. 1, no. 1(81), pp. 58–74, 2025. https://doi.org/10.15587/2706-5448.2025.323117

[33] A. Saeed, A. Alawi, M. H. Sharqawy, and M. A. Janaideh, "Advancements in temperature-sensing technologies for lithium-ion batteries in electric vehicle thermal management systems: A comprehensive review," *IEEE Sens. J.*, vol. 25, no. 23, pp. 42 442–42 461, 2025. https://doi.org/10.1109/JSEN.2025.3616085

[34] P. Nandy, A. F. Sandi, B. Ariantara, N. Abdullah, and T. M. I. Mahlia, "Performance of beeswax phase change material (PCM) and heat pipe as passive battery cooling system for electric vehicles," *Case Stud. Therm. Eng.*, vol. 21, no. 100655, 2020. https://doi.org/10.1016/j.csite.2020.100655

[35] D. K. Yadav, P. K. S. Rathore, R. K. Singh, A. K. Gupta, and B. S. Sikarwar, "Experimental study on paraffin wax and soya wax supported by high-density polyethylene and loaded with nano-additives for thermal energy storage," *Energies*, vol. 17, no. 11, p. 2461, 2024. https://doi.org/10.3390/en17112461

[36] A. Al-Masri, K. Khanafer, and K. Vafai, "Thermal modeling of porous medium integrated in PCM and its

application in passive thermal management of electric vehicle battery pack," *J. Appl. Phys.*, vol. 136, no. 3, p. 035001, 2024. https://doi.org/10.1063/5.0221003

[37] A. K. Nandy and K. Balasubramanian, "Performance of compound wavy microchannel heat sinks with varying wavelengths and amplitudes in terms of thermo-hydraulics," *Asia-Pac. J. Chem. Eng.*, vol. 20, no. 5, p. e70051, 2025. https://doi.org/10.1002/apj.70051

[38] R. David and D. Söffker, "A state machine-based approach for estimating the capacity loss of lithium-ion batteries," *Annu. Conf. PHM Soc.*, vol. 15, no. 1, pp. 1–9, 2023. https://doi.org/10.36001/phmconf.2023.v15i1.3450